Boundary-Layer Meteorol (2009) 132:59–81
DOI 10.1007/s10546-009-9391-5

ARTICLE

Temporal Oscillations in the Convective Boundary Layer Forced by Mesoscale Surface Heat-Flux Variations

Song-Lak Kang

Received: 20 June 2008 / Accepted: 21 April 2009 / Published online: 8 May 2009
© Springer Science+Business Media B.V. 2009

Abstract A theoretical approach suggests that the surface heterogeneity on a scale of tens of kilometres can generate mesoscale motions that are not in a quasi-stationary state. The starting point of the theoretical approach is the equations of horizontal velocity and potential temperature that are low-pass filtered with a mesoscale cut-off wavelength. The transition of the generated mesoscale motions from a quasi-stationary state to a non-stationary state occurs when horizontal advection is strong enough to level out the potential temperature gradient on the surface heterogeneity scale. Large-eddy simulations (LES) suggest that the convective boundary layer (CBL) changes to a non-stationary state when forced by a surface heat-flux variation of amplitude of $100\,\mathrm{W\,m^{-2}}$ or higher and a wavelength of the order of 10 km. Spectral analysis of the LES reveals that when the mesoscale motions are in a quasi-stationary state, the energy provided by the surface heat-flux variation remains in organized mesoscale motions on the scale of the surface variation itself. However, in a non-stationary state, the energy cascades to smaller scales, with the cascade extending down into the turbulence scale when the wavelength of the surface heat-flux variation is on a scale smaller than 100 times the CBL height. The energy transfer from the generated mesoscale motions to the CBL turbulence results in the absence of a spectral gap between the two scales. The absence of an obvious spectral gap between the generated mesoscale motions and the turbulence raises questions about the applicability of mesoscale models for studies on the effect of high-amplitude surface heterogeneity on a scale of tens of kilometres.

Keywords Boundary-layer parameterization · Energy cascade · Organized motions · Spectral gap · Surface heat-flux variation · Temporal oscillation

The National Center for Atmospheric Research is sponsored by the National Science Foundation.

S.-L. Kang (✉)
Advanced Study Program, National Center for Atmospheric Research, Boulder, CO 80307, USA
e-mail: songlak@ucar.edu

S.-L. Kang
Department of Meteorology, The Pennsylvania State University, University Park, PA 16802, USA

1 Introduction

The earth's surface, which is heterogeneous on all space and time scales, significantly influences weather and climate systems. To understand the effect of the surface heterogeneity on the atmosphere, numerous studies have been performed (for a literature review, see Pielke 2001). The most well-known phenomenon associated with surface heterogeneity is the sea-breeze circulation, and it is also well-known that contrasting one-dimensional surface heterogeneity on land, such as between irrigation/non-irrigation areas, bare/vegetated ground, and urban/rural regions, can generate sea-breeze-like circulations. The generated mesoscale motions are known by various names, including the "inland breeze" suggested by Mahrt et al. (1994a).

Analytical studies (e.g., Dal et al. 1991; Dalu and Pielke 1993) using a linearized equation set have suggested that the optimum heterogeneity scale needed to generate a well-organized inland breeze circulation is the local Rossby radius of deformation. The Rossby deformation radius is estimated to be a few hundred kilometres for typical mid-latitude atmospheric conditions (Pielke 2001). Many studies that have investigated the effect of surface heterogeneity on scales of a few hundred kilometres or larger have used numerical mesoscale models (MM), and given that the effective resolution of a grid model is about 4–7Δ (where Δ is the grid spacing: Lele 1992; Bryan et al. 2003; Skamarock 2004), organized mesoscale motions on a scale of a few hundred kilometres can be fully resolved with a grid spacing of tens of kilometres.

However, the features of atmospheric boundary-layer (ABL) structures modified by heterogeneity on a smaller scale of tens of kilometres may be different from those suggested by previous MM-based studies. For example, Chen and Avissar (1994) and Weaver (2004) suggested that mesoscale fluxes (i.e., the vertical transport of mesoscale scalar fluctuations by mesoscale vertical velocities) become comparable to or more significant than the turbulence fluxes, although observations of significant mesoscale fluxes are rare in the ABL over surface heterogeneity on a scale of tens of kilometres. The rareness of significant mesoscale fluxes is likely associated with smaller mesoscale vertical velocities than the observed turbulent vertical velocities (e.g., Mahrt et al. 1994a,b; LeMone and Coauthors 2002; Kang et al. 2007).[1]

As already mentioned, in order to explicitly resolve mesoscale motions on the surface heterogeneity scale of tens of kilometres or smaller, the grid spacing of a mesoscale model can be set at $l/\Delta \sim 1$ (where l is the scale of the energy-containing turbulence). The numerical region of $l/\Delta \sim 1$ has been named the "Terra Incognita" by Wyngaard (2004), though typical mesoscale models have not been designed to run within this "Terra Incognita". Mesoscale models assume the presence of a spectral gap between mesoscale and turbulent fluctuations, which justifies the application of ABL parameterization without considering the direct downscale cascade from mesoscale to turbulent fluctuations. Thus, large-eddy simulation (LES), which can explicitly resolve both mesoscale fluctuations and the energy-containing turbulent eddies in the convective boundary layer (CBL), is a more appropriate tool to investigate the CBL forced by surface heterogeneity on a scale of tens of kilometres.

LES has been successfully applied to the horizontally homogeneous CBL over the last 40 years since Deardorff (1970), and more recently, the application of LES has expanded to the ABL over a heterogeneous surface (e.g., Hadfield et al. 1991, 1992; Shen and Leclerc 1995; Avissar and Schmidt 1998; Letzel and Raasch 2003; Patton et al. 2005; Esau 2007;

[1] Typically, mesoscale vertical velocities are associated with horizontal convergence and divergence and turbulent vertical velocities are associated with static stability.

Kang and Davis 2008). Initially, these LES-based studies focused on surface heterogeneity on a scale comparable to the typical CBL height of 1 km (e.g., Hadfield et al. 1991, 1992; Shen and Leclerc 1995). With increasing computer resources, studies have increased the heterogeneity scale to more than ten times the CBL height (e.g., Avissar and Schmidt 1998; Letzel and Raasch 2003; Patton et al. 2005; Esau 2007; Kang and Davis 2008), finding that the surface heterogeneity on a scale of tens of kilometres generates mesoscale motions that can significantly modify CBL structures. Avissar and Schmidt (1998) assumed that the mesoscale motions generated by one-dimensional surface heat-flux variations are in a quasi-stationary state, but recent studies have found that the generated mesoscale motions may change to a non-stationary state (Letzel and Raasch 2003; Esau 2007; Kang and Davis 2008). Letzel and Raasch (2003) first found that the CBL forced by high-amplitude surface-heat flux variations may trigger temporal oscillations in thermally-induced mesoscale motions. They developed a conceptual hypothesis for the mechanism of temporally oscillating, thermally-induced mesoscale circulations: the circulation induced by the horizontal temperature gradient must be strong enough to level out part of the horizontal gradient and this effectively cuts off its own forcing. When the generated mesoscale circulation is weak enough, however, the horizontal gradient is rebuilt by the continuing surface heat-flux variation and the same cycle repeats. Letzel and Raasch (2003), however, focused more on the oscillation onset itself by using LES results rather than exploring the oscillation onset mechanism and the regimes where the oscillations occur. In addition, the temporal variation of the generated mesoscale motions found by Letzel and Raasch (2003) was not a pure but a damped oscillation, because the period and amplitude of the temporal variation change with time. However, the term 'temporal oscillation' from Letzel and Raasch (2003) will be used to denote the generated mesoscale motions in a non-stationary state.

Given that the onset of the temporal oscillation may considerably change CBL structures (Kang and Davis 2008), an in-depth explanation of the onset mechanism of the temporal oscillation is necessary. In Sect. 2, we establish that the temporal oscillation is a physically plausible phenomenon in the CBL forced by a one-dimensional, contrasting surface heat-flux distribution. The equations for potential temperature and horizontal velocity are scaled with a low-pass mesoscale filter. Then, in Sect. 3, the CBL is simulated using LES for a one-dimensional surface heat-flux variation. The comparison of the LES results with the theoretical explanation provides further insight into the transition of the generated mesoscale motions from a quasi-stationary state to a non-stationary state in the CBL forced by mesoscale surface heterogeneity on a scale of tens of kilometres.

2 Theoretical Approach

2.1 Surface Heat-Flux Variation and Variable Decomposition

An atmospheric variable ϕ is decomposed into a domain average $\langle\phi\rangle$ and the perturbation from the domain average ϕ', which will be referred as the total fluctuation, viz.

$$\phi(x_1, x_2; z, t) = \langle\phi\rangle(z, t) + \phi'(x_1, x_2; z, t). \tag{1}$$

In the horizontally homogeneous CBL, the total fluctuations are assumed to arise from small-scale turbulence. However, we prescribe a one-dimensional, mesoscale surface heat-flux variation that is sinusoidal with mean value $\langle F_{sfc}\rangle$, amplitude A_F, and mesoscale wavelength λ_F:

$$F_{sfc}(x_1) = \langle F_{sfc} \rangle + A_F \sin\left(\frac{2\pi}{\lambda_F} x_1\right). \tag{2}$$

In the CBL above this mesoscale surface heat-flux variation, the total fluctuation is assumed to have two components, a mesoscale fluctuation ϕ^M and a microscale (turbulence) fluctuation ϕ''.

$$\phi'(x_1, x_2; z, t) = \phi^M(x_1; z, t) + \phi''(x_1, x_2; z, t). \tag{3}$$

where the mesoscale mean is defined as

$$[\phi](x_1; z, t) = \langle \phi \rangle(z, t) + \phi^M(x_1; z, t). \tag{4}$$

Thus, the bracket denotes a low-pass filtered variable with a sharp cut-off filter in Fourier space (e.g., Moeng and Wyngaard 1988; Kim et al. 2002).

Using Eqs. 1, 3, and 4, the atmospheric variable ϕ in the horizontally heterogeneous CBL can be decomposed as

$$\phi(x_1, x_2; z, t) = [\phi](x_1; z, t) + \phi''(x_1, x_2; z, t). \tag{5}$$

2.2 $[u]$-Momentum and $[\theta]$ Equations

The filtered Navier–Stokes equation in a dry atmosphere, neglecting the Coriolis force and molecular viscosity terms, is written as

$$\frac{\partial u_i}{\partial t} + u_j \frac{\partial u_i}{\partial x_j} = -\frac{1}{\rho_0}\frac{\partial p}{\partial x_i} - \frac{\rho'}{\rho_0} g \delta_{3i} + \frac{1}{\rho_0}\frac{\partial \tau_{ij}}{\partial x_j}, \tag{6}$$

where p is the perturbation pressure, $\rho_0(z)$ is the base-state density satisfying hydrostatic balance, ρ' is the perturbation from the hydrostatic reference state, δ is the Kronecker delta, and τ_{ij} are the subgrid-scale fluxes produced by LES spatial filtering. In Eq. 6, $u_i (i = 1, 2, 3)$ are the filtered velocity components in the x_i direction, which are also denoted by u, v, and w, respectively.

The mesoscale flows appear to be generated only in the x_1 direction because the mesoscale surface heat-flux variation Eq. 2 is prescribed only in this direction and the Coriolis force is ignored. In order to derive scaling factors, by using Eq. 5 with the assumptions of $[v] \approx 0$ and $[w] \approx 0$, the u-momentum equation is decomposed into

$$\begin{aligned} &\frac{\partial [u]}{\partial t} + \frac{\partial u''}{\partial t} + [u]\frac{\partial [u]}{\partial x} + [u]\frac{\partial u''}{\partial x} + u_j''\frac{\partial [u]}{\partial x_j} + u_j''\frac{\partial u''}{\partial x_j} \\ &\quad = -\frac{1}{\rho_0}\frac{\partial [p]}{\partial x} - \frac{1}{\rho_0}\frac{\partial p''}{\partial t} + \frac{1}{\rho_0}\frac{\partial [\tau_{1j}]}{\partial x_j} + \frac{1}{\rho_0}\frac{\partial \tau_{1j}''}{\partial x_j}. \end{aligned} \tag{7}$$

After refiltering Eq. 7 with Eq. 5 and using $[\phi''] = 0$, $[[\phi]\phi''] = 0$, $[[\phi][\phi]] = [\phi][\phi]$ (the second and third relations are proved in the Appendix) and the commutative property of spatial averaging ($[\partial\phi/\partial t] = \partial[\phi]/\partial t$), the $[u]$-momentum equation becomes

$$\frac{\partial [u]}{\partial t} + [u]\frac{\partial [u]}{\partial x} + \frac{\partial}{\partial x_j}\left[u_j'' u'' - \frac{\tau_{1j}}{\rho_0}\right] = -\frac{1}{\rho_0}\frac{\partial [p]}{\partial x}. \tag{8}$$

Here, the direction of the surface heat-flux variation is defined as x_1 (or x) direction. Thus, the spatial gradients in Eq. 8 are defined along the direction the surface heterogeneity of Eq. 2 is prescribed. Also the zero-divergence assumption is used to obtain the third term on the

left-hand side of Eq. 8, an assumption that is valid when the vertical displacement is small compared to the density scale height (which is on the order of 10 km).

By using Eq. 5 also with the assumptions $[v] \approx 0$ and $[w] \approx 0$, the filtered potential temperature equation, neglecting the molecular diffusion term, is reduced to

$$\frac{\partial[\theta]}{\partial t} + \frac{\partial\theta''}{\partial t} + [u]\frac{\partial[\theta]}{\partial x} + [u]\frac{\partial\theta''}{\partial x} + u_j''\frac{\partial[\theta]}{\partial x_j} + u_j''\frac{\partial\theta''}{\partial x_j} + \frac{\partial\left[f_j\right]}{\partial x_j} + \frac{\partial f_j''}{\partial x_j} = 0, \tag{9}$$

where f_i is the subgrid-scale flux of potential temperature. Refiltering Eq. 9 with Eq. 5 yields

$$\frac{\partial\left[\theta\right]}{\partial t} + [u]\frac{\partial[\theta]}{\partial x} + \frac{\partial}{\partial x_j}\left[u_j''\theta'' + f_j\right] = 0, \tag{10}$$

where it should be noted that the simplified Eqs. 8 and 10 are written only for deriving scaling parameters in this section, and not for the numerical model used in Sect. 3.

2.3 Mesoscale Potential Temperature Gradient

In Fig. 1, the sub-domain ($0 \leq x < \lambda_F/2$) where the surface heat flux is above the domain average ($F_{sfc} \geq \langle F_{sfc}\rangle$) is defined as the warmer region and the sub-domain ($\lambda_F/2 \leq x < \lambda_F$) where the surface heat flux is below the domain average ($F_{sfc} \leq \langle F_{sfc}\rangle$) is the cooler region. It is hypothesized that the driving force for the surface-heterogeneity-induced horizontal flows in the lower CBL is the potential temperature gradient at a given scale of surface heat-flux variation, namely the potential temperature gradient between the warmer and cooler regions.

To estimate the potential temperature gradient, we assume horizontal homogeneity in the warmer and cooler regions. In the warmer region, by using the horizontal homogeneity assumption, Eq. 10 can be written as

$$\frac{\partial\overline{\theta}^W}{\partial t} \approx -\frac{\partial\overline{F}^W}{\partial z}, \tag{11}$$

where $\overline{\phi}^W$ represents the spatial average of ϕ over the warmer region and $F \equiv w''\theta'' + f_3$.

By integrating Eq. 11 vertically through the well-mixed CBL in the warmer region, one can obtain the local time evolution of the vertically-averaged mixed-layer potential temperature,

$$\frac{\partial\overline{\theta}_{ML}^W}{\partial t} \approx \frac{\overline{F_{sfc}}^W - \overline{F_{z_i}}^W}{\overline{z_i}^W} \approx (1-\alpha)\,\frac{\overline{F_{sfc}}^W}{\overline{z_i}^W}, \tag{12}$$

where $\overline{\theta}_{ML}^W$ indicates a mixed-layer average potential temperature and $\overline{z_i}^W$ is the CBL height averaged over the warmer region. In Eq. 12, it is assumed that the heat flux at $\overline{z_i}^W$ is expressed as a constant fraction of the value at the surface ($\alpha = \overline{F_{z_i}}^W / \overline{F_{sfc}}^W$; Stull 1988). After applying the horizontal homogeneity assumption to the cooler region, the mixed-layer potential temperature gradient between the warmer and cooler regions can be approximated as

$$\delta\theta_{ML} \equiv \bar{\theta}_{ML}^W - \bar{\theta}_{ML}^C \approx \alpha'\frac{A_F}{\langle z_i\rangle}t, \tag{13}$$

where $\alpha' \equiv 1.27(1-\alpha)$, and 1.27 is the difference of the means of the sine function between $0-\pi$ and $\pi-2\pi$. In Eq. 13, $A_F = \overline{F_{sfc}}^W - \overline{F_{sfc}}^C$ is used and $\langle z_i\rangle = 0.5(\overline{z_i}^W + \overline{z_i}^C)$ is assumed, as illustrated in Fig. 1.

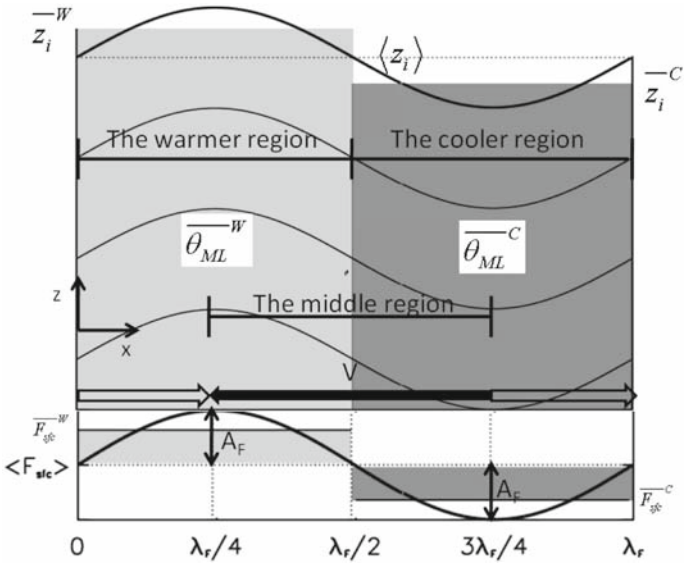

Fig. 1 Schematic diagram of the ABL over a one-dimensional sinusoidal surface heat-flux variation. *Top*: vertical cross-section, where *thin solid contours* are isotherms. *Bottom*: surface heat flux, F_{sfc}; $\langle F_{sfc} \rangle$, A_F, and λ_F represent mean, amplitude, wavelength of the surface heat-flux variation, respectively. $\overline{F_{sfc}}^W$ and $\overline{\theta_{ML}}^W$ are local-mean surface heat flux and mixed-layer potential temperature averaged over the warmer region. $\overline{F_{sfc}}^C$ and $\overline{\theta_{ML}}^C$ are averaged over the cooler region. V represents the magnitude of the surface-heterogeneity-induced horizontal velocity and z_i the ABL height

The growth of the potential temperature gradient between the warmer and cooler regions aids the development of a horizontal pressure gradient. As Fig. 1 depicts, there are two middle regions: (1) $\lambda_F/4 \leq x < 3\lambda_F/4$, (2) $x \leq \lambda_F/4$ or $x > 3\lambda_F/4$. The middle region is defined as the sub-domain composed of half of the warmer region and half of the cooler region. According to Eq. 8, this pressure gradient generates horizontal velocities, specifically horizontal flows across the middle regions. In the following, to simplify the discussion, only the middle region $\lambda_F/4 \leq x < 3\lambda_F/4$ will be considered with the assumption of similarity between the two middle regions.

As the generated mesoscale horizontal flow increases, the temperature advection by the generated mesoscale flows (the second term in the left-hand side of Eq. 10) may not be negligible. Because the mesoscale horizontal flow is from the cooler region to the warmer region (Fig. 1), there is cold advection in the lower CBL. This cold advection acts to reduce the potential temperature gradient.

It is hypothesized that a balanced state between the growth of the temperature gradient by differential surface heating and the decay of the gradient by temperature advection is reached, and express this balance as

$$-\frac{\langle F_{z_i} \rangle - \langle F_{sfc} \rangle}{\langle z_i \rangle} \approx V \frac{\delta \theta_{ML}}{(\lambda_F/2)}, \tag{14}$$

where V represents the magnitude of the generated horizontal velocity and λ_F is a given heterogeneity scale. Making use of Eqs. 13 and 14, one can estimate the time required for the temperature advection to become large enough to balance the vertical flux divergence,

$$\tau_b \approx \frac{\langle F_{sfc} \rangle}{1.27 A_F} \frac{\lambda_F}{2V} = 0.8 \gamma \tau_v, \tag{15}$$

where $\gamma \equiv \langle F_{sfc} \rangle / A_F$ is the ratio of the domain-averaged surface heat flux to the amplitude of the surface heat-flux variation, and τ_v is the time required for the generated mesoscale horizontal flow to travel over the middle region (i.e., the advection time scale; $\tau_v \equiv \lambda_F / 2V$). Based on Eq. 15, one concludes that for higher amplitude surface heat-flux variation (larger A_F), the time τ_b required to reach equilibrium between temperature advection and vertical flux divergence is smaller.

One can also hypothesize that horizontal advection could go beyond a point of equilibrium, reducing the potential temperature gradient and weakening the horizontal flow at a given heterogeneity scale. The potential temperature advection would then decrease, and eventually the potential temperature gradient would again intensify through the time-invariant surface differential heating described by Eq. 2. This would result in an oscillatory mesoscale flow, as first found by Letzel and Raasch (2003).

2.4 Critical Velocity Scale V_c

In this section, we attempt to obtain an estimate of the critical scale of the generated mesoscale horizontal velocity (V) that initiates a temporally-oscillating mesoscale flow. First, in terms of scaling variables, the [u]-momentum equation (Eq. 8) is written as

$$\frac{V}{\tau_e} + V \frac{V}{L} + \frac{u_t^2}{l} = \frac{1}{\rho_o} \frac{P}{L} \tag{16}$$

where τ_e is the Eulerian time scale, u_t and l are the velocity and length scales of energy-containing turbulent eddies, P is the characteristic pressure scale, and L is the characteristic horizontal scale, here $0.5\lambda_F$.

Figure 2 illustrates the time evolution of the magnitude of the mesoscale horizontal velocity generated by a surface heat-flux variation strong enough to initiate the temporal oscillation. At the oscillation onset, assuming that the Eulerian time scale τ_e and the advection time scale $\tau_v \equiv \lambda_F / 2V$ are the same order of magnitude, one can write that

$$\frac{V}{\tau_e} = \frac{V}{\lambda_F / 2V}. \tag{17}$$

Before the oscillation onset, at a given wavelength and amplitude of the surface heat- flux variation, τ_v becomes smaller with time due to the growth of V, but τ_e seems not to change with time given the similar growth rates of $V$and the pressure gradient force in

$$\tau_e \approx V \left(\frac{1}{\rho_0} \frac{P}{L} \right)^{-1}. \tag{18}$$

At an earlier time when V is smaller, the advection time scale (τ_v) is larger than the Eulerian time scale (τ_e); in other words, the advection terms, the second terms on the left-hand side of both Eqs. 8 and 10, are still negligible. A linear approach ignoring the advection term or using a constant horizontal velocity for the advection term (e.g., Rotunno 1983; Dal et al. 1991, 1996, 2000; Wang et al. 1996; Baldi et al. 2008) may be appropriate if the amplitude (A_F) of the surface heat-flux variation is not large enough for V to grow to the point where Eq. 17 is satisfied (V_c in Fig. 2). When τ_v becomes smaller than τ_e, the advection terms cannot be ignored. As discussed in the previous section, the horizontal temperature advection reduces

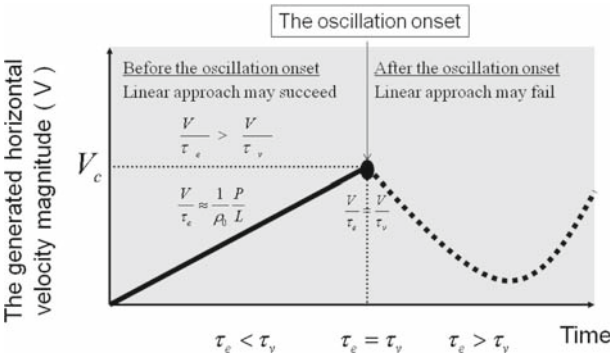

Fig. 2 Illustration for the critical velocity scale V_c, a threshold for the onset of the temporal oscillation in the surface-heterogeneity-induced horizontal flows. The τ_e represents the Eulerian time scale and the τ_v the advection time scale. The *thick solid line* represents the generated horizontal velocity that is in a quasi-stationary state and the *thick dotted line* represents the horizontal velocity that is temporally oscillatory. Before the temporal oscillation onset, there exists a spectral gap between a given heterogeneity scale and the turbulence scale, which is demonstrated in Fig. 6a

the temperature gradient between the warmer and cooler regions, a necessary condition for the onset of the temporal oscillation in the generated horizontal flows.

Next we hypothesize that when the advection term is equal to the smaller-scale flow term, this defines a critical velocity, V_c that must be attained in order to initiate temporally-oscillating horizontal flows. From Eq. 16,

$$\frac{2V_c^2}{\lambda_F} = \frac{u_t^2}{l}. \tag{19}$$

In Eq. 19, the smaller-scale fluctuations are assumed to be characterized with a typical size (l) and velocity (u_t) of energy-containing turbulent eddies, which are scaled to the mixed-layer depth (z_i) and the convective velocity scale (w_*), respectively. In other words, for the microscale (turbulent) fluctuations in the horizontally heterogeneous CBL, characteristics of mixed-layer similarity (Lenschow et al. 1980) are assumed to be retained until the point of $\tau_e = \tau_v$ (Fig. 2). Thus, using $l \approx c_z z_i$ and $u_t \approx c_u w_*$, where c_z and c_u are coefficients to be determined, Eq. 18 can be rewritten as

$$V_c \approx c\sqrt{\lambda_F / z_i}\, w_*, \tag{20}$$

where $c \equiv c_u/\sqrt{2c_z}$. Lenschow et al. (1980) demonstrate that $c_u = 0.4$ and Kaimal et al. (1976) that $c_z = 1.5$. Thus, the coefficient c in Eq. 20 is estimated at 0.2. If the mesoscale velocity that is generated by the surface heat-flux variation exceeds the critical velocity scale, the oscillatory horizontal flows that are as significant in magnitude as turbulent flows can be initiated. This hypothesis is evaluated using numerical simulations in the next section.

3 Numerical Experiment and Results

3.1 Simulated CBL

The Bryan–Fritsch model (Bryan and Fritsch 2002) is used with the one-dimensional single scale surface heat-flux variation of Eq. 2. The surface heat-flux variation is represented by a sinusoidal function with amplitudes (A_F) in the range from 50 to 200 W m^{-2} and wavelengths

Table 1 Parameters characerizing the set of all cases

Case	A_F (W m^{-2})	λ_F (km)	$D_{x1} \times D_{x2}$ (km^2)	Forecast time (h)
A200L128	200	128	128×5	12
A200L64	200	64	64×5	6
A200L32	200	32	32×5	6
A200L16	200	16	32×5	6
A200L08	200	8	32×5	6
A125L128	125	128	128×5	12
A125L64	125	64	64×5	12
A125L32	125	32	32×5	6
A125L16	125	16	32×5	6
A125L08	125	8	32×5	6
A050L128	50	128	128×5	12
A050L64	50	64	64×5	12
A050L32	50	32	32×5	12
A050L16	50	16	32×5	12
A050L08	50	8	32×5	12
A000L00	0	0	32×5	6

A_F and λ_F represent the amplitude and wavelength of the surface heat-flux variation (2) respectively. The D_{x1} and D_{x2} are the horizontal dimensions of the model domain in the x_1 and x_2 directions respectively. The mean surface flux $\langle F_{sfc} \rangle$ is 240 W m^{-2}

(λ_F) from 8 to 128 km. The Bryan–Fritsch model was developed as a cloud-resolving model using LES techniques (Bryan et al. 2003) and it has been used to solve a range of nonlinear problems (e.g., Bannon et al. 2006; Bryan and Rotunno 2008). The model has examined the impact of mesoscale surface heterogeneity on the mesoscale and microscale (turbulence) structure of the CBL (Kang and Davis 2008).

The domain-average value $\langle F_{sfc} \rangle$ of the surface heat flux is set at 240 W m^{-2}, and the various amplitudes A_F and wavelengths λ_F of the surface heat-flux variation prescribed for simulating the horizontally heterogeneous CBL are summarized in Table 1.

Since our study addresses the onset of the temporal oscillation, which considerably changes the CBL structure according to Kang and Davis (2008), the numerical set-up is similar to Kang and Davis (2008). In order to identify the temporal oscillation onset, the model integration time is as long as 12 h. The horizontal grid spacing is 100 m, and the vertical grid spacing is 10 m up to 100 m above the ground, linearly increases from 10 to 40 m between 100 and 1,900 m, and then remains constant at 40 m up to the model top of 3,500 m. The model domain varies from 32 to 128 km in the x_1 (or x) direction and is 5 km in the x_2 (or y) direction. The surface flux variation is prescribed only in the x_1 direction, and at the initial time, random perturbations of 0.1 K that initiate development of three-dimensional turbulent flows are superimposed on the potential temperature at the lowest atmospheric level. In both horizontal directions, the lateral boundary conditions are periodic.

The upper boundary is a flat, rigid wall with a Rayleigh damping layer (Durran and Klemp 1983) occupying 1 km beneath the model top. The lower boundary is also a flat, rigid surface. Unlike the prescribed surface heat flux, the surface momentum flux is derived from a simple surface-drag parameterization (Stull 1988).

Soundings of potential temperature and water vapour mixing ratio are obtained from the rawinsonde released at the Homestead site (36.55°N, 100.6°W) at about 1130 LST on 25 May 2002. The initial potential temperature is constant (296 K) at altitudes less than 626 m,

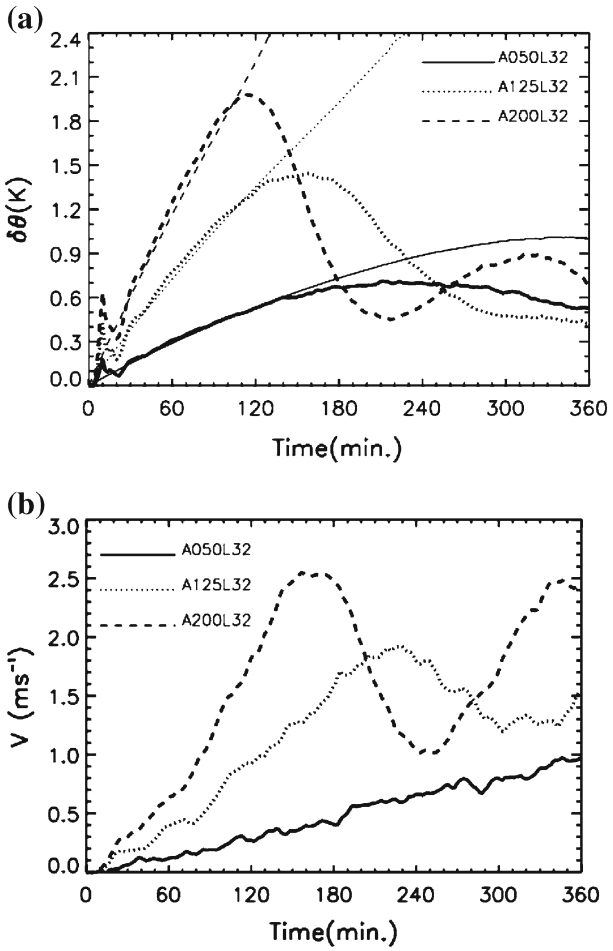

Fig. 3 The time evolution of **a** the potential temperature gradient at 95 m agl between the warmer and cooler regions, and **b** the magnitude of the generated horizontal velocity at 95 m agl for cases with the variation amplitudes of 50 (A050L32), 125 (A125L32), and 200 (A200L32) $\mathrm{W\,m^{-2}}$ at the variation wavelength of 32 km. The *thin lines* in **a** indicate the estimates of the potential temperature gradient by using Eq. 13

and increases at the rate of $34.8\,\mathrm{K\,km^{-1}}$ between 626 and 806 m. Above 806 m, the potential temperature increases at the rate of $3.8\,\mathrm{K\,km^{-1}}$. The initial CBL height is 716 m.

3.2 Parameters of the Oscillation Onset

For cases with different amplitudes of 50, 125, and $200\,\mathrm{W\,m^{-2}}$ at $\lambda_F = 32\,\mathrm{km}$, the potential temperature gradients between the warmer and cooler regions at 95 m above the ground level (agl) are presented in Fig. 3a. Figure 3a also shows the linear estimate (Eq. 13) of the potential temperature gradient, which ignores the temperature advection. The deviation of the LES temperature gradients from the linear estimate of Eq. 13 implies that the temperature advection becomes too significant to be negligible.

In Fig. 3a, the potential temperature gradient for a higher amplitude variation case more rapidly decreases from the peaks of the time series, compared with that for a lower amplitude

variation case. Figure 3b presents the generated horizontal wind speed averaged over the middle region. The temporal oscillation of horizontal wind speed has a time lag of 40–70 min from the oscillation of potential temperature gradient. In this study, the point at which the generated horizontal wind speed starts to decrease is defined as the temporal oscillation onset. If the time of the oscillation onset is used as a reference time, the rate of wind speed fluctuation is likely comparable between different cases.

For cases with wavelengths from 8 to 128 km at $A_F = 200\,\mathrm{W\,m^{-2}}$ the generated horizontal wind speeds at 95 m that are averaged over the middle region are shown in Fig. 4a, where it is demonstrated that the surface heat-flux variation with the high amplitude of $200\,\mathrm{W\,m^{-2}}$ generates the temporal oscillation in the horizontal flows. With a shorter wavelength variation, the oscillation onset is earlier, the amplitude of the oscillation is smaller, and the periodicity and lifetime of the oscillation are shorter. This is in agreement with Letzel and Raasch (2003), who came to the same conclusion based on the oscillation of perturbation energy (Figs. 6 and 8 therein) for wavelengths between 5 and 30 km. Figure 4b demonstrates that the surface heat-flux variation with the low amplitude of $50\,\mathrm{W\,m^{-2}}$ generates no temporal oscillation in the horizontal flows within the 12-h integration period except for the case with the shortest wavelength of 8 km in our numerical experiment.

Both Avissar and Schmidt (1998) and Patton et al. (2005) suggested that a well-organized inland breeze circulation is basically in a quasi-stationary state. Avissar and Schmidt (1998) found that surface heat-flux variations with a relatively long wavelength of 20–40 km generate well-organized circulations. In contrast, Patton et al. (2005) suggested that the relatively short wavelength of 5–15 km generates the well-organized circulations in their numerical simulations.

Figures 3 and 4 demonstrate that the results of Avissar and Schmidt (1998) and Patton et al. (2005) are partially consistent with our result. Figure 3b demonstrates that the horizontal wind speed generated by the surface heat-flux variation with the wavelength of 32 km and the amplitudes of 50–$200\,\mathrm{W\,m^{-2}}$ steadily grows until 2 h 40 min after the introduction of the surface forcing. Before the oscillation onset, at about 3 h, the highest amplitude of $200\,\mathrm{W\,m^{-2}}$ of the surface heat-flux variation at the wavelength of 32 km generates the strongest horizontal wind speed of $2.0\,\mathrm{m\,s^{-1}}$ (Fig. 3b).

Avissar and Schmidt (1998) analyzed their results averaged over 1.5–2.5 h after the surface forcing activation, and found that the highest amplitude of $250\,\mathrm{W\,m^{-2}}$ at the wavelength of 40 km generates the strongest horizontal wind speed of 2–$4\,\mathrm{m\,s^{-1}}$ in their numerical experiment (Fig. 3 of Avissar and Schmidt 1998). In our case (Fig. 4a), the highest amplitude of $200\,\mathrm{W\,m^{-2}}$ at a shorter wavelength of the surface heat-flux variation initiates the temporal oscillation for their averaged period of 1.5–2.5 h. Thus, the slightly different averaging period changes the optimum wavelength for generating the well-organized mesoscale circulation.

Patton et al. (2005), however, indirectly prescribed the surface heat-flux variation with the low amplitude of $40\,\mathrm{W\,m^{-2}}$ in their LES. Figure 4b shows that the horizontal wind speeds generated by the surface heat-flux variation with the amplitude of $50\,\mathrm{W\,m^{-2}}$ increases at least until 8 h after the surface forcing activation. Thus, the mesoscale circulation in Patton et al. (2005) is likely in a quasi-stationary state up to 8 h as well as in their averaging period of 1–3 h.

In order to determine the time and the intensity of the oscillation onset of the generated horizontal flows, the model has been run until the oscillation onset within the 12-h integration period for all the cases. The horizontal wind speed at the oscillation onset of the generated horizontal flows at 95 m agl is presented in Fig. 5a. We use the critical velocity scale of Eq. 20 to provide guidance for the oscillation onset. In computing the critical velocity scale, we use the values of =736 m and =$0.77\,\mathrm{m\,s^{-1}}$ from the horizontally homogeneous CBL case (A000L00).

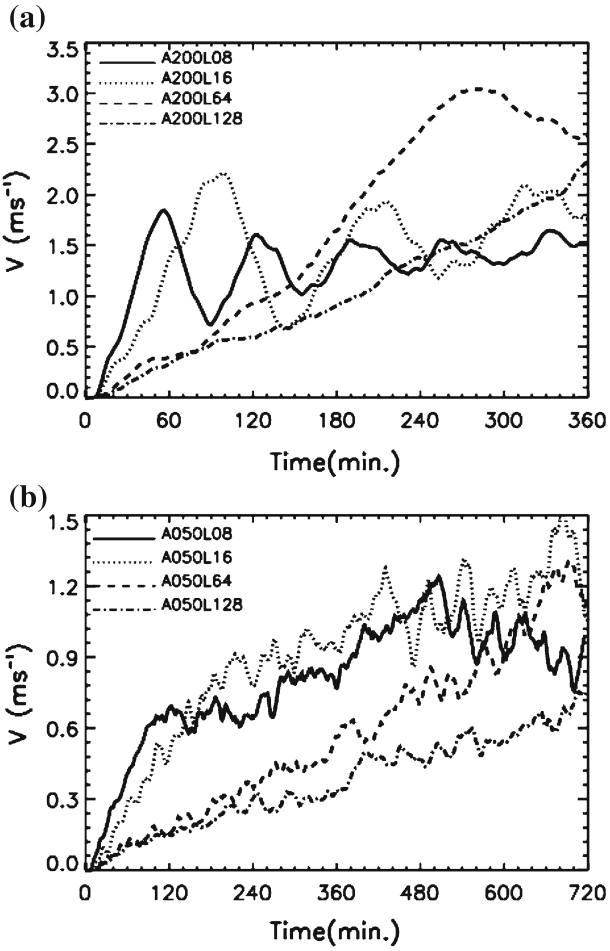

Fig. 4 The time evolution of the generated horizontal velocity at 95 m agl for cases with the variation wavelengths of 8, 16, 64, and 128 km at the variation amplitudes of **a** 200 W m^{-2} and **b** 50 W m^{-2}

For all the cases that initiate the temporal oscillation within the 12-h period, the generated horizontal wind speeds at their oscillation onsets are larger than the critical velocity scales (Fig. 5a). Also, the horizontal wind speed at the oscillation onset increases as λ_F increases. Thus, at the oscillation onset, the two hypotheses used to determine the critical velocity scale (Eq. 20) seem to be valid: (1) the Eulerian time scale is comparable to the advection time scale, and (2) the microscale (turbulence) fluctuations in the horizontally heterogeneous CBL is still characterized using the turbulence statistics from the homogenous CBL.

The time taken for the generated horizontal flows at 95 m agl to initiate the temporal oscillation in presented in Fig. 5b. The horizontal flows generated by a shorter-wavelength and higher-amplitude surface heat-flux variation initiate the temporal oscillation at an earlier time, as already demonstrated in Figs. 3b and 4a. Given the time scale of the Coriolis parameter, the assumption of no Coriolis force used in this study is valid up to 4 h at middle latitudes. The LES results presented in Fig. 5b suggest that within the time limit of 4 h, for the horizontal flows to be oscillatory, the wavelength of the surface heat-flux variation

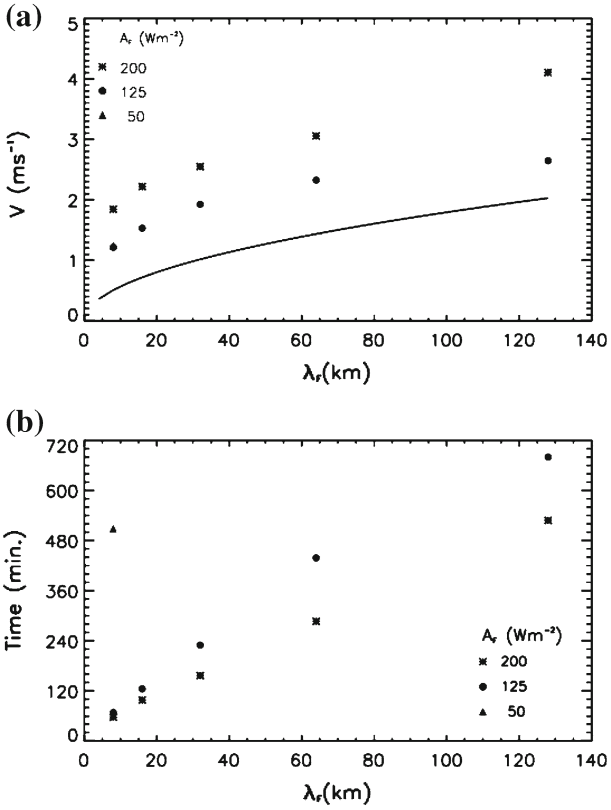

Fig. 5 **a** The magnitude of the generated horizontal velocity at 95 m agl at the oscillation onset and **b** the time when the onset of the temporal oscillation occurs for every case. The *solid line* **a** represents the critical velocity scale as a function of the wavelength of the surface heat-flux variation

should be shorter than 50 km at a variation amplitude higher than 100 W m^{-2}. However, if the variation amplitude is lower than 50 W m^{-2}, or the variation wavelength is longer than 50 km, the generated horizontal flows seem to be in a quasi-stationary state within the time period of 4 h.

3.3 Spectral Analysis

In the previous section, the potential temperature at 95 m averaged over the warmer and cooler regions is used to evaluate the horizontal potential temperature gradient, and the horizontal wind speed at 95 m averaged over the middle region is used for the generated horizontal wind speed. In spectral space, however, the averaged values of potential temperature and horizontal velocity may contain multiple scale fluctuations; in other words, although the surface heat-flux variation is described by a Fourier series with non-zero amplitude only at a given heterogeneity scale as shown in Eq. 2, the atmospheric fluctuations forced by the mesoscale surface heterogeneity should be expressed by a Fourier series with non-zero amplitudes at multiple scales. It is hypothesized that the atmospheric fluctuations at a given surface heterogeneity scale cascade to smaller scales at the oscillation

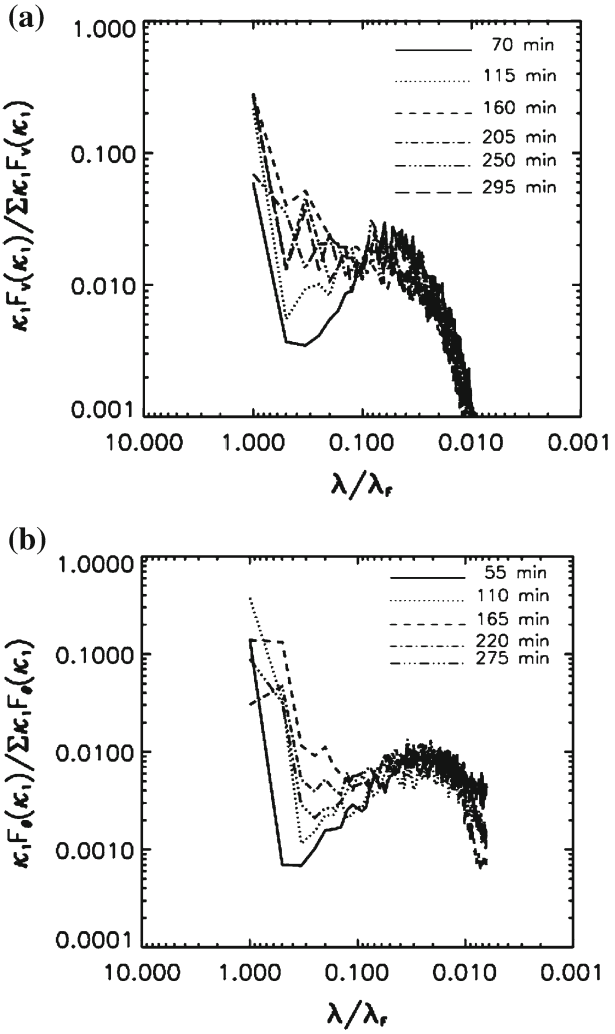

Fig. 6 **a** One-dimensional horizontal velocity spectra at 95 m above ground level at times of 70, 115, 160, 205, 250, and 295 min and **b** potential temperature spectra at times of 55, 110, 165, 220, 275 min for case A200L32. The temporal oscillation onset occurs at 160 min

onset, which is defined as the point at which the generated horizontal wind speed starts to decrease.

At times of 70, 115, 160, 205, 250, and 295 min for case A200L32, the normalized spectra of horizontal velocity at 95 m agl are presented in Fig. 6a. These one-dimensional spectra are obtained by integrating two-dimensional spectral densities along the x_2 direction at the specified times, which are around the onset of the temporal oscillation. Note that times of 70 and 115 min occur before the oscillation onset, the time of 160 min is at the oscillation onset, and the times of 205, 250, and 295 min. occur after the oscillation onset (Fig. 3b).

Before the oscillation onset, the spectral gap between the mesoscale and microscale fluctuations is obvious at $\lambda/\lambda_F = 0.4$. Figure 6a shows that the horizontal velocity spectra have

two significant spectral density peaks: one at the heterogeneity scale of $\lambda/\lambda_F = 1$, and the second at the turbulence scale of $\lambda/\lambda_F = 0.05$, which is about $1.5z_i$. However, after the oscillation onset, the spectral densities at $0.5 \leq \lambda/\lambda_F \leq 1$ significantly increase and the spectral gap between the mesoscale and microscale (turbulent) fluctuations becomes ambiguous.

At later times after the oscillation onset, the spectral densities between $0.5 \leq \lambda/\lambda_F \leq 1$ are small again and the spectral densities at $\lambda/\lambda_F = 1$(i.e., the given heterogeneity scale) are also smaller than before. In other words, the reduction of the horizontal velocity fluctuations occurs both at the given heterogeneity scale $\lambda_F/\lambda = 1$ and in the scale range between $0.5 \leq \lambda/\lambda_F \leq 1$. In contrast, the spectral densities in the turbulence scale range are somewhat larger compared with values at earlier times (but after the oscillation onset). Kang et al. (2007) suggested that cold advection in the lower CBL and warm advection in the upper CBL result in somewhat statistically stable structures in the domain-averaged vertical profiles of potential temperature over heterogeneous surfaces (Fig. 3 therein). Thus, from the perspective of the domain-averaged statistics, the heterogeneous CBL reduces buoyancy and decreases the intensity of turbulence throughout the model domain (Kang and Davis 2008). The spectra in Fig. 6 demonstrate that after the oscillation onset horizontal wind fluctuations are reduced, and turbulence is increased. The increased turbulence is associated with the increased stability, resulting from the lower-level cold advection and upper-level warm advection (for details, see Sect. 4b of Kang and Davis (2008)).

The spectra of potential temperature in Fig. 6b show that, at the time of the highest potential temperature gradient at $\lambda/\lambda_F = 1$, specifically at 110 min, the mesoscale fluctuations at $0.5 \leq \lambda/\lambda_F \leq 1$ are less significant than is the case at later times when the potential temperature gradients at $\lambda/\lambda_F = 1$ are lower. At 165 min, the mesoscale fluctuations at $0.5 \leq \lambda/\lambda_F \leq 1$ are the most significant whereas the fluctuations at $\lambda/\lambda_F = 1$ are lower compared with the spectra at the earlier time. Thus, at the oscillation onset (namely 160 min) and at the given heterogeneity scale the transfer of the fluctuations to smaller scales is likely the most significant for both potential temperature and horizontal velocity. However, unlike the horizontal velocity spectra, the spectral gap between the mesoscale and microscale fluctuations is found at $0.5 \leq \lambda/\lambda_F \leq 1$ even after the oscillation onset in the potential temperature spectra.

The atmospheric disturbance due to the surface heterogeneity on a scale of the order of 10 km seems to directly extend to the microscale (turbulent) fluctuations. For cases with the variation wavelengths of 8, 16, 32, 64, and 128 km at the variation amplitude of 200 $\mathrm{W\,m^{-2}}$, the horizontal velocity spectra at the oscillation onset times are exhibited in Fig. 7. Except for the longest wavelength case (A200L128), which exhibits a somewhat obvious spectral gap around $0.03 \leq \lambda/\lambda_F \leq 0.1$ (about 4–13 km), the horizontal velocity spectra have no significant spectral gap between the mesoscale and microscale (turbulent) fluctuations. In other words, only the spectrum from A200L128, which has the surface heterogeneity on a scale of the order of 100 km, has two clearly separated spectral peaks. For the other cases with a shorter wavelength with surface heat-flux variation, there are no obvious spectral gaps.

Using LES with the surface heat-flux variation for wavelengths of 16 and 32 km and various amplitudes, Kang and Davis (2008) showed that the microscale (turbulence) structure of the heterogeneous CBL in quasi-steady horizontal flows retains characteristics of mixed-layer similarity. For the CBL with high amplitude variation, mixed-layer similarity is violated even when mesoscale fluctuations are filtered out. Their conclusion that non-stationary characteristics of mesoscale fluctuations may directly influence the microscale fluctuation characteristics is consistent with our results for the case with a variation wavelength of 64 km or shorter.

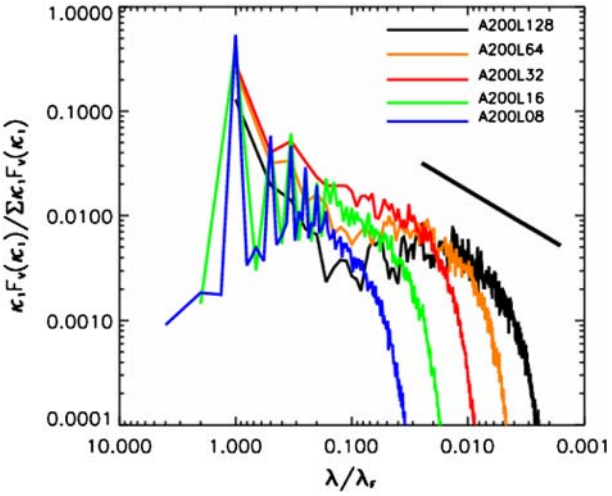

Fig. 7 One-dimensional horizontal velocity spectra at 95 m above ground level at the oscillation onset for the cases with the variation wavelengths of 128, 64, 32, 16, 8 km at the variation amplitude of 200 W m^{-2}. The *short thick line* represents the $\kappa^{-2/3}$ spectrum

3.4 Spectral Decomposition

In order to isolate the mesoscale fluctuations, the LES results are transformed into Fourier spectral space. Two cut-off wavelengths are used: (1) one half of a given heterogeneity scale (λ_H), and (2) λ_T for the turbulence scale: $\lambda_T = 4$ km is selected, as in the observational studies on the horizontally heterogeneous CBL (e.g., Mahrt and Gibson 1992; Mahrt et al. 1994a,b, Finkele et al. 1994; LeMone et al. 2007; Kang et al. 2007).

θ^M and v_1^M from a non-oscillatory case with $A_F = 50$ W m^{-2} and $\lambda_F = 128$ km (Fig. 8) are compared with those from an oscillatory case in which $A_F = 200$ W m^{-2} and $\lambda_F = 128$ km (Fig. 9). In order to define the mesoscale fluctuations at the given heterogeneity scale $\lambda_F = 128$ km and for the scale range between the given heterogeneity scale and the turbulence scale, two cut-off wavelengths are used: (1) $\lambda_H = 64$ km (*contoured*), and (2) $\lambda_T = 4$ km (*shaded*). For both non-oscillatory and oscillatory cases, the horizontal gradients of θ^M low-pass filtered with λ_H (θ_H) decrease after approximately 300 min. However, compared with the non-oscillatory case (A050L128), the gradient of θ_H reduces much more rapidly for the oscillatory case (A200L128). For the non-oscillatory case (A050L128), v_1^M low-pass filtered with λ_H (v_H) continuously increases, whereas for the oscillatory case (A200L128) the v_H increases until 520 min but decreases after that time.

For the non-oscillatory case (A050L128), θ^M and v_1^M low-pass filtered with λ_T appear as random fluctuations superimposed on the mesoscale fluctuations at the given heterogeneity scale (Fig. 8). However, for the oscillatory case (A200L128), for the fields of θ^M and v_1^M with λ_T, a strong potential temperature gradient and its associated significant horizontal convergence exist at the centre of the warmer region, $x_1 = -32$ km, from a time of about 360 min (Fig. 9).

In order to see in detail processes related to the strong potential temperature gradient and horizontal velocity convergence at the mesoscale smaller than the given heterogeneity scale, θ^M and v_1^M with λ_T are compared with those with λ_H at 280, 400, 520, and 640 min

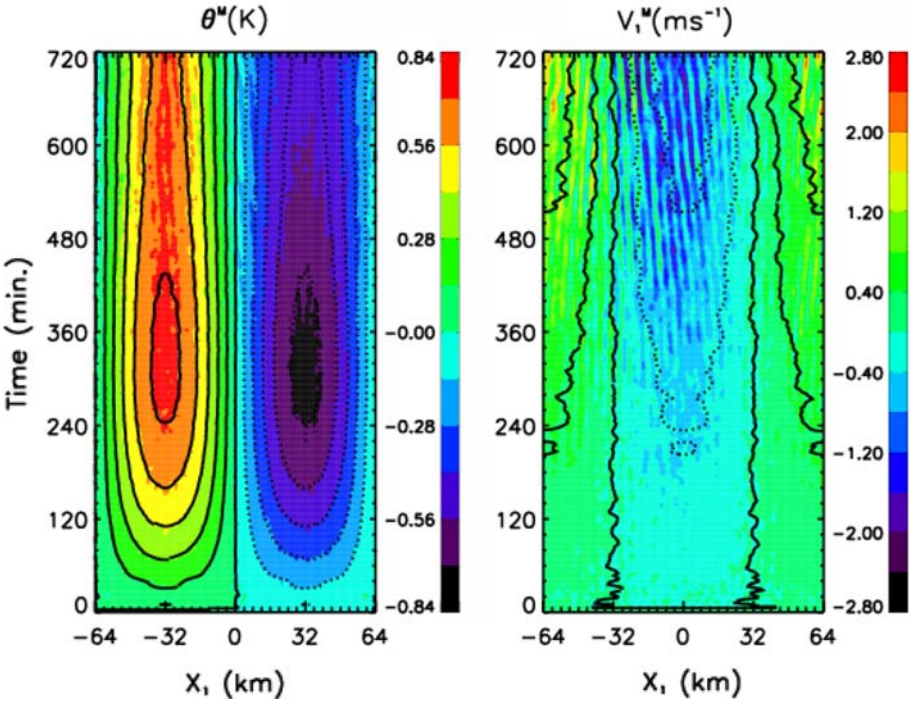

Fig. 8 Time series of **a** the mesoscale fluctuations of potential temperature θ^M at 95 m agl that are low-pass filtered with the cut-off wavelength of $\lambda_H = 64$ km (*contoured*) or $\lambda_T = 4$ km (*shaded*). The contour intervals are: −0.70, −0.56, −0.42, −0.28, −0.14, 0, 0.14, 0.28, 0.42, 0.56, and 0.70 K; **b** the mesoscale fluctuations of horizontal velocity v_1^M at 95 m agl that are low-pass filtered with the cut-off wavelength of $\lambda_H = 64$ km (*contoured*) or $\lambda_T = 4$ km (*shaded*). The contour intervals are: −0.8, −0.4, 0, 0.4, 0.8,m s^{-1} for A050L128

in Fig. 10. In Fig. 10a, the comparison of θ^M using λ_H or λ_T demonstrates more cooling around the edge of the warmer region and more warming at the centre of the warmer region. Figure 10b shows that there is a strong horizontal convergence at the centre of the warmer region ($x_1 = -32$ km) in v_1^M with λ_T between 400 and 520 min. The strong convergence is associated with a significant vertical velocity at $x_1 = -32$ km (Fig. 11a), which is absent in the non-oscillatory case (Fig. 11b).

4 Conclusions

The transition of the CBL from a quasi-stationary state to a non-stationary state over mesoscale surface heat-flux variations has been theoretically analyzed. We took as the starting point the equations of horizontal velocity and potential temperature that were low-pass filtered with a mesoscale cut-off wavelength. The non-stationary state begins with the onset of a temporal oscillation of the mesoscale motions generated by the surface heterogeneity. The oscillation, as defined by the first maximum in V, occurs at the time when horizontal advection is strong enough to decrease the potential temperature gradient at the heterogeneity scale. Thus, at the oscillation onset, the Eulerian time scale is equal to the advection time scale in the equations of horizontal velocity and potential temperature.

We suggest the horizontal velocity scale that must be attained to initiate temporally oscillating flows, and estimate the critical value to be proportional to the square root of the

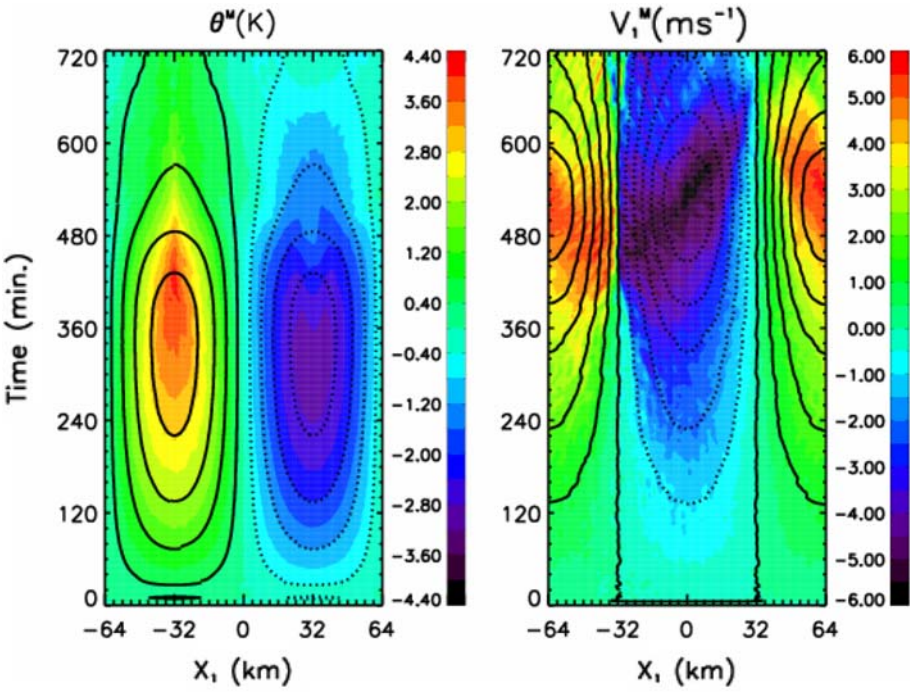

Fig. 9 Time series of **a** the mesoscale fluctuations of potential temperature low-pass filtered with the cut-off wavelength of $\lambda_H = 64$ km (*contoured*) and $\lambda_T = 4$ km (*shaded*). The contour intervals are: −2.8, −2.0, −1.2, −0.4, 0.4, 1.2, 2.0, 2.8 K; **b** the mesoscale fluctuations of horizontal velocity v_1^M low-pass filtered with the cutoff wavelength of $\lambda_H = 64$ km (*contoured*) and $\lambda_T = 4$ km (*shaded*). The contour intervals are: −5, −4, −3, −2, −1, 0, 1, 2, 3, 4, 5 m s^{-1} for A200L128

wavelength of the surface heat-flux variation normalized with the CBL height. The critical velocity scale hypothesizes two conditions at the oscillation onset: (1) the Eulerian time scale is comparable to the advection time scale, and (2) the characteristic size and velocity of the energy-containing turbulent eddies are comparable with those found typically in a horizontally homogeneous CBL. The second hypothesis is associated with the fact that at the oscillation onset the total fluctuations in the CBL forced by mesoscale surface heterogeneity can be decomposed into, (i) a mesoscale fluctuation at a given heterogeneity scale and, (ii) a microscale fluctuations that is characterized with the turbulence statistics from the homogeneous CBL.

Large-eddy simulations were performed with surface heat flux varying sinusoidally in the x-direction with an average value of 240 W m^{-2} and amplitudes that ranged from 50 to 200 W m^{-2}, and wavelengths from 8 to 120 km. The LES results demonstrate that at the oscillation onset the magnitude of the generated horizontal velocity is larger than the critical velocity scale. The generated horizontal wind speed at the oscillation onset increases with variation wavelength at a rate similar to the critical velocity scale. The agreement of the LES results with the theoretical critical velocity scale suggests that the two hypotheses used in the theory are likely valid at least at the oscillation onset.

LES spectra demonstrate that the decrease of horizontal velocity magnitude at the heterogeneity scale is associated with a momentum cascade to smaller scales. In particular, in all cases with a given heterogeneity scale smaller than 100 km (about $100 z_i$), the atmospheric

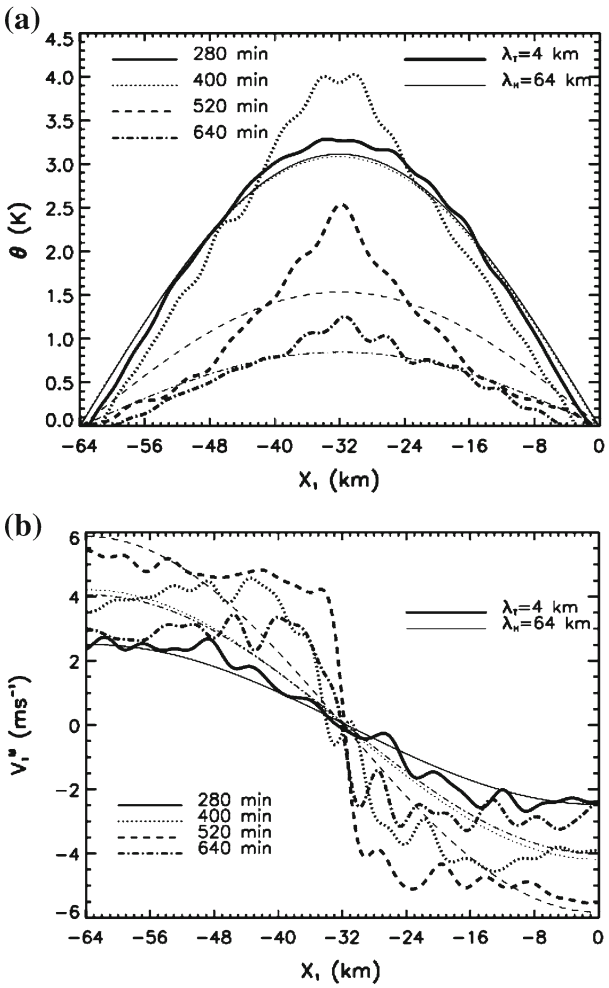

Fig. 10 Mesoscale fluctuations of **a** potential temperature θ^M and **b** horizontal velocity v_1^M at 95 m above ground level in the warmer region at 280, 400, 520, and 640 min for case A200L128. The *thick lines* are obtained using the cut-off wavelength $\lambda_T = 4$ km and the *thin lines* are using the cut-off wavelength of $\lambda_H = 64$ km. The temporal oscillation occurs at 520 min

fluctuations forced by mesoscale surface heterogeneity seem to cascade down to the microscale (turbulent) fluctuations without any significant spectral gap between the mesoscale and microscale (turbulent) fluctuations. In the LES results, a generation of fluctuations on a scale smaller than the surface heterogeneity scale is evident at the centre of the warmer region at the oscillation onset, with a significant gradient of potential temperature, a sharp change of horizontal velocity and direction, considerable vertical velocity associated with horizontal convergence, and a substantial change in the CBL height.

The oscillation onset is likely the start of a break-up process of atmospheric fluctuations at the heterogeneity scale into smaller-scale fluctuations. In the CBL forced by the surface heat-flux variation on a scale of the order of 10 km, and with an amplitude of 100 $\mathrm{W\,m^{-2}}$ or higher, the mesoscale fluctuations at a given surface heterogeneity scale are continuously transferred down to the small-scale turbulence. In other words, any significant spectral gap between the mesoscale and microscale (turbulent) fluctuations is absent in the CBL forced by the mesoscale surface heterogeneity. The basic strategy of mesoscale modelling is to explicitly compute mesoscale fluctuations but to parameterize microscale (turbulent) fluctuations.

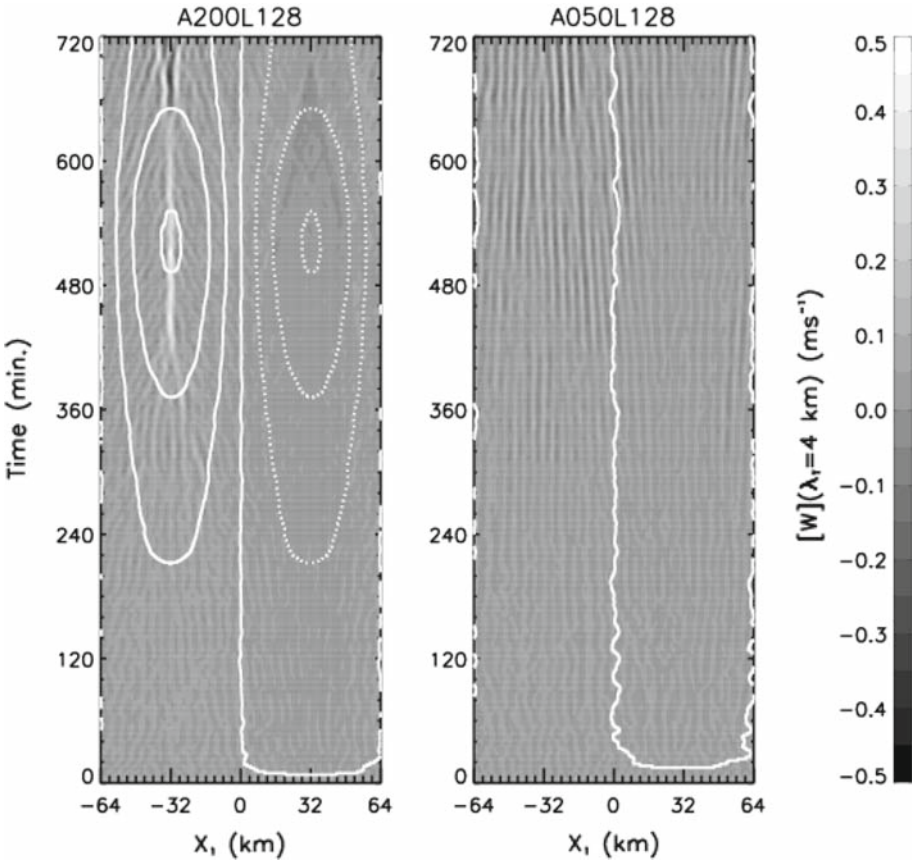

Fig. 11 Time series of the mesoscale fluctuations of vertical velocity w^M at 95 m that are low-pass filtered with the cut-off wavelength of $\lambda_H = 64$ km (*contoured*) or $\lambda_T = 4$ km (*colour shaded*) for cases **a** A200L128 and **b** A050L128. The contour intervals are: −0.03, −0.02, −0.01, 0, 0.01, 0.02, 0.03 m s^{-1}

Thus, before the oscillation onset, the strategy of mesoscale modelling is likely to work. However, after the oscillation onset the strategy is not sufficient to describe adequately the CBL forced by mesoscale surface heterogeneity.

Therefore, this result raises a question about the applicability of mesoscale models to investigate the effect of mesoscale surface heterogeneity on the atmosphere. However, the conclusions from the simulated CBL with simple, idealized surface and atmospheric conditions (temporally constant with a one-dimensional variation of surface heat flux, cyclic lateral boundary conditions, and flat terrain) are insufficient to generally question the applicability of ABL parameterization in a mesoscale model in the presence of surface heterogeneity effects. Thus, the temporal oscillation onset and its resultant energy cascade process need to be investigated further with more realistic surface and atmospheric conditions.

Acknowledgments The author appreciates the helpful comments provided by Drs. Peggy LeMone, George Bryan, Ethan Gutmann, Tom Horst, and Russ Schumacher, and thanks Drs. Ken Davis, John Wyngaard, and Brain Reen who read and commented on an earlier version of this manuscript. This study was supported by NSF Grant ATM 0130349, and DTRA Grant W911NF 0610439, and by the Advanced Study Program of NCAR. The author wishes to thank two anonymous reviewers for their helpful comments on the manuscript.

Appendix

Proofs of $[[f(x)]f''(x)] = 0$ and $[[f(x)]f(x)] = [[f(x)]f(x)]$ used in Sect. 2

First, we represent a function $f(x)$ as a complex Fourier series, $f(x) = \sum_{n=1}^{N} \hat{f}(\kappa_n) e^{i\kappa n^x}$, where $\hat{f}(\kappa_n)$ are coefficients that are complex numbers. This function can be decomposed into low-pass filtered components $[f(x)] = \sum_{n=1}^{c} \hat{f}(\kappa_n)\, e^{i\kappa n^x}$, (where c is a cut-off wavelength) and high-pass filtered components $f''(x) = \sum_{n=c+1}^{N} \hat{f}(\kappa_n) e^{i\kappa n^x}$, by the wave cut-off filter [ ]. The product of these low- and high-pass parts can be written as

$$[f(x)]f''(x) = \hat{f}(\kappa_1)\hat{f}(\kappa_{c+1}) e^{i(\kappa_1+\kappa_{c+1})x} + \cdots + \hat{f}(\kappa_c)\hat{f}(\kappa_N) e^{i(\kappa_c+\kappa_N)x}. \tag{21}$$

Applying the wave cut-off filter to this product yields

$$[[f(x)]]f''(x) = \left[\hat{f}(\kappa_1)\hat{f}(\kappa_{c+1}) e^{i(\kappa_1+\kappa_{c+1})x} + \cdots + \hat{f}(\kappa_c)\hat{f}(\kappa_N) e^{i(\kappa_c+\kappa_N)x}\right]. \tag{22}$$

In (22), if $\kappa_1 + \kappa_{c+1} > \kappa_c$ then $[[f(x)]f''(x)] = 0$. The condition $\kappa_1 + \kappa_{c+1} > \kappa_c$ is always true because $\kappa_{c+1} > \kappa_c$ and $\kappa_1 > 0$.

Second, the product of two low-pass filtered components of the function $f(x)$ can be written as

$$[f(x)][f(x)] = \hat{f}(\kappa_1)\hat{f}(\kappa_1) e^{i(\kappa_1+\kappa_1)x} + \cdots + \hat{f}(\kappa_c)\hat{f}(\kappa_N) e^{i(\kappa_c+\kappa_c)x}, \tag{23}$$

and applying the wave cut-off filter to this product yields

$$\begin{aligned}[f(x)][f(x)] &= [\hat{f}(\kappa_1)\hat{f}(\kappa_1) e^{i(\kappa_1+\kappa_1)x} + \cdots + \hat{f}(\kappa_c)\hat{f}(\kappa_N) e^{i(\kappa_c+\kappa_c)x}] \\ &= [f(x)][f(x)]\end{aligned} \tag{24}$$

References

Avissar R, Schmidt T (1998) An evaluation of the scale at which ground-surface heat flux patchiness affects the convective boundary layer using a large-eddy simulation model. J Atmos Sci 55:2666–2689. doi:10.1175/1520-0469(1998)055<2666:AEOTSA>2.0.CO;2

Baldi M, Dalu GA, Pielke RA Sr (2008) Vertical velocities and available potential energy generated by landscape variability—theory. J Appl Meteorol Climatol 47:397–410. doi:10.1175/2007JAMC1539.1

Bannon PR, Chagnon JM, James RP (2006) Mass conservation and the anelastic approximation. Mon Weather Rev 134:2989–3005. doi:10.1175/MWR3228.1

Bryan GH, Fritsch JM (2002) A benchmark simulation for moist nonhydrostatic numerical models. Mon Weather Rev 130:2917–2928. doi:10.1175/1520-0493(2002)130<2917:ABSFMN>2.0.CO;2

Bryan GH, Rotunno R (2008) Gravity currents in a deep anelastic atmosphere. J Atmos Sci 65:536–556. doi:10.1175/2007JAS2443.1

Bryan GH, Wyngaard JC, Fritsch JM (2003) Resolution requirements for the simulation of deep moist convection. Mon Weather Rev 131:2394–2416. doi:10.1175/1520-0493(2003)131<2394:RRFTSO>2.0.CO;2

Chen F, Avissar R (1994) The impact of land-surface wetness heterogeneity on mesoscale heat fluxes. J Appl Meteorol 33:1323–1340. doi:10.1175/1520-0450(1994)033<1323:TIOLSW>2.0.CO;2

Dalu GA, Pielke RA (1993) Vertical heat fluxes generated by mesoscale atmospheric flow induced by thermal inhomogeneities in the PBL. J Atmos Sci 33:919–926. doi:10.1175/1520-0469(1993)050<0919:VHFGBM>2.0.CO;2

Dalu GA, Pielke RA, Avissar R, Kallos G, Baldi M, Guerrini A (1991) Linear impact of thermal inhomogeneities on mesoscale atmospheric flow with zero synoptic wind. Ann Geophys 9:641–647

Dalu GA, Pielke RA, Baldi M, Zeng X (1996) Heat and momentum fluxes induced by thermal inhomogeneities with and without large-scale flow. J Atmos Sci 53:3286–3302. doi:10.1175/1520-0469(1996)053<3286:HAMFIB>2.0.CO;2

Dalu GA, Pielke RA Sr, Vidale PL, Baldi M (2000) Heat transport and weakening of atmospheric stability induced by mesoscale flows. J Geophys Res 105:9349–9363. doi:10.1029/1999JD901064

Deardorff JW (1970) Convective velocity and temperature scales for the unstable planetary boundary layer and for Rayleigh convection. J Atmos Sci 27:1211–1213. doi:10.1175/1520-0469(1970)027<1211:CVATSF>2.0.CO;2

Durran DR, Klemp JB (1983) A compressible model for the simulation of moist mountain waves. Mon Weather Rev 111:2341–2361. doi:10.1175/1520-0493(1983)111<2341:ACMFTS>2.0.CO;2

Esau IN (2007) Amplification of turbulent exchange over wide Arctic leads: large-eddy simulation study. J Geophys Res 112:D08109. doi:10.1029/2006JD007225

Finkele K, Hacker JM, Kraus H, Byron-Scott RAD (1994) A complete sea-breeze circulation cell derived from aircraft observations. Boundary-Layer Meteorol 73:299–317. doi:10.1007/BF00711261

Hadfield MG, Cotton WR, Pielke RA (1991) Large-eddy simulations of thermally forced circulations in the convective boundary layer. Part I: a small-scale circulation with zero wind. Boundary-Layer Meteorol 57:79–114. doi:10.1007/BF00119714

Hadfield MG, Cotton WR, Pielke RA (1992) Large-eddy simulations of thermally forced circulations in the convective boundary layer. Part II: the effect of changes in wavelength and wind speed. Boundary-Layer Meteorol 58:307–327. doi:10.1007/BF00120235

Kaimal J, Wyngaard J, Haugen D, Cote O, Izumi Y, Caughey S, Readings C (1976) Turbulence structure in the convective boundary layer. J Atmos Sci 33:2152–2169. doi:10.1175/1520-0469(1976)033<2152:TSITCB>2.0.CO;2

Kang S-L, Davis K (2008) The effects of mesoscale surface heterogeneity on the fair-weather convective atmospheric boundary layer. J Atmos Sci 65:3197–3213. doi:10.1175/2008JAS2390.1

Kang S-L, Davis KJ, LeMone M (2007) Observations of the ABL structures over a heterogeneous land surface during IHOP_2002. J Hydrometeorol 8:221–244. doi:10.1175/JHM567.1

Kimmel SJ, Wyngaard JC, Otte MJ (2002) "Log-Chipper" turbulence in the convective boundary layer. J Atmos Sci 59:1124–1134. doi:10.1175/1520-0469(2002)059<1124:LCTITC>2.0.CO;2

Lele SK (1992) Compact finite difference schemes with spectral-like resolution. J Comput Phys 103:16–42. doi:10.1016/0021-9991(92)90324-R

LeMone MA, Grossman RL, Mcmillen RT, Liou K-N, Ou SC, Mckeen S, Angevine W, Ikeda K, Chen F (2002) CASE-97: late-morning warming and moistening of the convective boundary layer over the Walnut River Watershed. Boundary-Layer Meteorol 104:1–52. doi:10.1023/A:1015569104180

LeMone MA, Chen F, Alfieri JG, Tewari M, Geerts B, Miao Q, Grossman RL, Coulter RL (2007) Influence of land cover and soil moisture on the horizontal distribution of sensible and latent heat fluxes in southeast Kansas during IHOP_2002 and CASES-97. J Hydrometeorol 8:68–87. doi:10.1175/JHM554.1

Lenschow D, Wyngaard J, Pennell W (1980) Mean-field and second-moment budgets in a baroclinic, convective boundary layer. J Atmos Sci 37:1313–1326. doi:10.1175/1520-0469(1980)037<1313:MFASMB>2.0.CO;2

Letzel MO, Raasch S (2003) Large eddy simulation of thermally induced oscillations in the convective boundary layer. J Atmos Sci 60:2328–2341. doi:10.1175/1520-0469(2003)060<2328:LESOTI>2.0.CO;2

Mahrt L, Gibson W (1992) Flux decomposition into coherent structures. Boundary-Layer Meteorol 60:143–168. doi:10.1007/BF00122065

Mahrt L, Sun J, Vickers D, Macpherson JI, Pederson JR, Desjardins RL (1994a) Observations of fluxes and inland breezes over a heterogeneous surface. J Atmos Sci 51:2484–2499. doi:10.1175/1520-0469(1994)051<2484:OOFAIB>2.0.CO;2

Mahrt L, Desjardins R, Macpherson JI (1994b) Observations of fluxes over heterogeneous surfaces. Boundary-Layer Meteorol 67:345–367. doi:10.1007/BF00705438

Moeng CH, Wyngaard JC (1988) Spectral analysis of larger-eddy simulations of the convective boundary layer. J Atmos Sci 45:3573–3587. doi:10.1175/1520-0469(1988)045<3573:SAOLES>2.0.CO;2

Patton EG, Sullivan PP, Moeng C-H (2005) Influence of idealized heterogeneity on wet and dry planetary boundary layers coupled to the land surface. J Atmos Sci 62:2078–2097. doi:10.1175/JAS3465.1

Pielke RA (2001) Influence of the spatial distribution of vegetation and soils on the prediction and soils on the cumulus convective rainfall. Rev Geophys 39:151–177. doi:10.1029/1999RG000072

Rotunno R (1983) On the linear theory of the land and sea breeze. J Atmos Sci 40:1999–2009. doi:10.1175/1520-0469(1983)040<1999:OTLTOT>2.0.CO;2

Shen S, Leclerc MY (1995) How large must surface inhomogeneities be before they influence the convective boundary layer structure? A case study. Q J Roy Meteorol Soc 121:1209–1228. doi:10.1002/qj.49712152603

Skamarock WC (2004) Evaluating mesoscale NWP models using kinetic energy spectra. Mon Weather Rev 132:3019–3032. doi:10.1175/MWR2830.1

Stull RB (1988) An introduction to boundary layer meteorology. Kluwer Academic Publishers, Dordrecht, 666 pp

Wang J, Bars RL, Eltahir EA (1996) A stochastic linear theory of mesoscale circulation induced by the thermal heterogeneity of the land surface. J Atmos Sci 53:3349–3366. doi:10.1175/1520-0469(1996)053<3349:ASLTOM>2.0.CO;2

Weaver CP (2004) Coupling between large-scale atmospheric processes and mesoscale land–atmosphere interactions in the U.S. Southern Great Plains during summer. Part II: mean impacts of the mesoscale. J Hydrometeorol 5:1247–1258. doi:10.1175/JHM-397.1

Wyngaard JC (2004) Toward numerical modeling in the "Terra Incognita". J Atmos Sci 16:1816–1826. doi:10.1175/1520-0469(2004)061<1816:TNMITT>2.0.CO;2